ORIGINAL PAPER

Solid-state pseudocapacitors based on MnO₂-nanorod-electrodes and plastic crystal incorporated gel polymer electrolyte: synergistic effect of Li-salt addition in electrolyte and morphology of electrodes

Md. Yasir Bhat [1] · S. A. Hashmi [1]

Abstract

We present a novel configuration of high-performance solid-state pseudocapacitors, fabricated with symmetric MnO₂-nanorod-electrodes, prepared via chemical and hydrothermal routes, and plastic crystals-based gel polymer electrolytes (GPEs). Comparative studies are reported on capacitors employing GPEs comprising a mixture of non-ionic plastic crystal succinonitrile (SN) and organic ionic plastic crystal (OIPC) 1-ethyl-1-methylpyrrolidinium bis(trifluoromethylsulfonyl)imide (EMPTFSI), without and with Li-salt (LiTFSI), entrapped in a co-polymer poly(vinylidine fluoride-co-hexafluoropropylene) (PVdF-HFP). The MnO₂-nanorods have been characterized for their morphological/structural aspects, specific surface area, and porosity and correlated the characteristics with their capacitive performance. Clean and uniform morphology and high surface area with mesoporous character are found to be responsible factors for superior supercapacitive performance of hydrothermally derived MnO₂-nanorod-electrodes as compared to chemically derived MnO₂-nanorods. Lithium salt incorporation in GPE has been found to be another important factor to improve the pseudoapacitive performance of the cells due to facile intercalation/ extraction of Li-ions through MnO₂-electrodes. The optimum performance of the pseudocapacitor cell has been observed in terms of specific capacitance (98–101 F g^{-1}), specific energy (~ 13.7 W h kg^{-1}), and maximum specific power (~ 32.6 kW kg^{-1}) as observed from charge-discharge studies, due to synergistic effect of morphology of hydrothermally derived MnO₂-nanorod-electrodes and incorporation of Li-ions in GPE. The hydrothermally derived MnO₂-nanorod-electrodes also exhibit high rate capability; however, it reduces significantly when Li-salt incorporated GPE is employed. The optimum cell exhibits almost stable cyclic performance up to ~ 3300 charge-discharge cycles after only ~ 17% fading in specific capacitance for initial few cycles.

Keywords MnO₂-nanorods · Pseudocapacitors · Plastic crystals · Gel polymer electrolyte · Impedance analysis · Cyclic voltammetry

Introduction

Interest in the development of alternative energy storage/ conversion devices with high energy/power densities has increased worldwide in the present scenario of day-to-day demands, depleting fossil fuels and environment-related issues. Electrochemical capacitors (ECs) and lithium ion batteries

✉ S. A. Hashmi
sahashmi@physics.du.ac.in; hashmisa2002@yahoo.co.in

[1] Department of Physics and Astrophysics, University of Delhi, Delhi 110007, India

(LIBs) are the current devices of interest and under extensive development due to their use in various applications, including portable electronic appliances, medical utilities, uninterruptible power supplies, and electrical and hybrid electrical vehicles (EVs and HEVs) [1–3]. Particularly, ECs are the power sources, which are extensively reported as alternative to rechargeable batteries/LIBs due to various reasons, including their simple design, high power density, and long cycle life [1, 2, 4, 5]. Based on charge storage mechanisms, ECs are classified in two broad categories: (i) EDLCs (electric double layer capacitors) and (ii) pseudocapacitors (redox capacitors) [4–6]. EDLCs, in general, employ carbonaceous electrode materials and store electrostatic charges, whereas pseudocapacitors are fabricated with transition metal oxides (TMOs)/mixed transition metal oxides (MTMOs) or conducting polymers [4–8] as electrodes and fast Faradaic

reaction(s) at electrode-electrolyte interfaces are responsible for pseudocapacitance.

Out of several reports on TMO-based pseudocapacitive electrodes, hydrated RuO_2 is noted to be the most promising as it offers very high specific capacitance than carbonaceous materials and it shows excellent redox activity and electrochemical stability [7, 9]. However, the high cost and its effective performance, restricted with acidic electrolytes only such as sulfuric acid, limit the extensive application of RuO_2 as supercapacitive electrodes and prompted researchers to focus on the alternative TMOs, e.g., NiO, CoO_x, SnO_2, MnO_2, and IrO_2 [4, 7, 10–17]. MnO_2, particularly, is a potential pseudocapacitive oxide, which is widely reported in literature due to its cost-effectiveness and promising electroactive behavior. MnO_2, as pseudocapacitor electrodes, are reported in bulk form, different nanostructured forms and its composites/ nanocomposites with carbonaceous materials, other oxides, and conducting polymers [15, 16, 18]. The capacitive performance of MnO_2 is generally tested in neutral electrolyte systems, which is another important advantage over other oxide electrodes, e.g., $RuO_2 \cdot xH_2O$ [15, 16].

MnO_2 has been synthesized via different techniques, namely thermal decomposition, sol-gel method, simple reduction, co-precipitation method, and low-cost electrodeposition method [19–25]. Jeong and Manthiram reported the synthesis of MnO_2 by the reduction of $KMnO_4$ using sodium hypophosphite, sodium dithionate, and potassium borohydride [20]. Kim and Papov prepared Pb- and Ni-mixed MnO_2 by the reduction of $KMnO_4$ with Mn/Ni/Pb acetate solutions [19]. Lee et al. synthesized MnO_2 at different temperatures from 300 to 1000 °C by a simple thermal decomposition of finely ground $KMnO_4$ powder [26]. Simple precipitation of MnO_2 has been achieved by mixing aqueous solutions of $MnSO_4$ and $KMnO_4$ [27] or $KMnO_4$ and $(CH_3COO)_2Mn$ [28]. The hydrothermal technique to prepare MnO_2 is very advantageous over the other chemical methods due to its ability to control their different nanostructural forms, such as nanoparticles, nanorods, nanourchins, and nanotubes by choosing proper time of reaction or temperature or solvent used [29, 30]. It may be noted that each nanostructure has its own activity, depending upon their morphology, when employed as electrodes in capacitors/batteries.

MnO_2 crystallizes in different structures with MnO_6 octahedra assemblies showing 1D, 2D, or 3D arrangements [31]. Materials with 1D nanostructure have sufficiently high surface area, small distance from surface to interior bulk, and smallest dimension, responsible to minimize ion diffusion path and very effective electrical transport continuity. This is the reason of increasing interest these days in the fabrication of 1D nano-MnO_2, such as MnO_2 nanowires [31–34] and nanorods [34, 35]. Further, MnO_2 has many polymorphs, namely α-, β-, γ-, δ-, and λ-MnO_2, and attracts ample attention because of their applications in batteries [36–40], catalysis [41, 42], ion

exchange [43, 44], etc. Wang et al. [32] have reported the synthesis of 1D α-MnO_2 single crystal nanowires and nanorods via hydrothermal method through the oxidation of $MnSO_4$ by $(NH_4)_2S_2O_8$ or $KMnO_4$, respectively. Li et al. [45] have synthesized well-aligned α-MnO_2 nanowires by electrochemical step-edge decoration. Also, α-MnO_2 nanorods with uniform diameter were prepared by Sugantha et al. through a sol-gel synthetic route [35].

Electrolyte is another important component, which plays a vital role in the charge storage processes of supercapacitors [6, 7, 46, 47]. Particularly for the pseudocapacitors based on TMO-electrodes, one of the important factors is the size of electrolyte ion(s), which should match with the size of structural tunnels of oxide electrodes for their possible insertion/ extraction. The electrochemical stability window (ESW) of an electrolyte is the other important factor, which limits the cell voltage of the supercapacitors. Thus, the careful selection of suitable electrolyte is of prime significance in view of its high ionic conductivity and wider potential window with sufficient thermal stability. Different liquid electrolytes (aqueous, organic, or ionic liquids) are found appropriate for MnO_2-based capacitors [48]. The MnO_2-based pseudocapacitors are generally characterized in neutral electrolytes, e.g., aqueous solutions of Na_2SO_4 and K_2SO_4 [20, 22, 28, 49]. However, liquid electrolytes show common problems in supercapacitors and batteries, such as limited transportability, bulky design, corrosion of electrodes/substrates, electrolyte leakage, and dissolution of active electrode materials [6, 46, 47, 49].

The gel polymer electrolytes (GPEs) that are basically liquid electrolytes entrapped in suitable host polymers, e.g., poly(vinylidinefluoride-co-hexafluoropropylene) (PVdF-HFP), poly(methyl methacrylate) (PMMA), polyacrylonitrile (PAN), and poly(vinyl alcohol) (PVA), are recently reported to be excellent substitute of liquid electrolytes for energy storage devices [6, 46, 47, 50]. Properties like high ionic conductivity comparable to liquid electrolytes, wide electrochemical stability, dimensional stability, and quasi-solid-state nature with excellent mechanical flexibility make the GPEs attractive over liquid electrolytes [6, 46, 47, 50–52]. Different GPEs are reported for supercapacitor applications comprising aqueous, organic solvent(s) or ionic liquid-based liquid electrolytes, immobilized in host polymers, e.g., PVA/H_2SO_4, PVA/H_3PO_4, (PVdF-HFP)/EC/PC/$LiClO_4$, PMMA/EC/PC/$NaClO_4$, (PVdF-HFP)/1-ethyl-3-methylimidazolium bis(tri-fluoromethylsulfonyl)imide (EMITFSI)/LiTFSI [46, 47, 50–52]. All of them have their own merits and demerits depending on their thermal and electrochemical stabilities and other factors related to safety issues like flammability, volatility, and toxicity [49, 50, 53]. The non-ionic plastic crystal succinonitrile (SN) has recently been introduced as a solid solvent/plasticizer in polymer-based electrolytes/GPEs [53–57], which have been proved to be potential electrolytes in solid-state batteries and supercapacitors. The SN, which is a waxy solid, can accommodate different ionic salts or ionic liquids

to become ionic conductors [58], and the mixture can be immobilized in different host polymers to form GPEs [53–57]. The organic ionic plastic crystals (OIPCs) are another class of materials, which form potential ionic conductors, when added with different Li/Na-salts [59–63]. Such electrolytes have the additional ability to accommodate the mechanical stress during the charge-discharge process of the devices like batteries/supercapacitors [59].

Despite their excellent electrochemical and mechanical properties, GPEs are rarely employed as electrolytes in MnO_2-based supercapacitors, except a very few reports [64, 65]. A symmetric flexible solid-state supercapacitor based on MnO_2-electrodes with GPE comprising polyvinylpyrrolidone (PVP)/$LiClO_4$ has been reported, which possesses high operating voltage of 1.6 V with high energy density and power density [64]. Our group presented the comparative performance characteristics of pseudocapacitors fabricated using electrochemically synthesized MnO_2-polypyrrole composite electrodes and three different electrolytes, namely aqueous PVA/H_3PO_4 polymer electrolyte, liquid electrolyte ($LiClO_4$/PC), and GPE (PMMA/EC/PC/$NaClO_4$) [18]. Lee et al. recently reported MnO_2 supercapacitors with potassium polyacrylate-co-polyacrylamide GPEs containing aqueous solution of KCl, which exhibited improvement (> 50%) in specific capacitance of the MnO_2-electrodes [65].

This paper reports the studies on MnO_2-nanorod based solid-state pseudocapacitors fabricated with GPEs containing a mixture of non-ionic plastic crystal and OIPC, SN and 1-ethyl-1-methylpyrrolidinium bis(trifluoromethylsulfonyl)imide (EMPTFSI), respectively, immobilized in poly(vinyidine fluoride-co-hexafluoropropylene) (PVdF-HFP). Morphological, structural, and porosity analyses have been performed to characterize MnO_2-nanorods to be employed as pseudocapacitive electrodes and correlated the observations with capacitive performance of the devices. The pseudocapacitor cells have been tested through electrochemical impedance spectroscopy (EIS), cyclic voltammetry (CV), and galvanostatic charge-discharge tests for numerous cycles. Studies are mainly focused to examine the effect of (i) morphology of MnO_2-nanorod-electrode materials, prepared by chemical and hydrothermal methods, and (ii) lithium salt addition in GPE composition PVdF-HFP/SN/EMPTFSI on the performance characteristics of pseudocapacitors. To the best of our knowledge, MnO_2-based capacitors with plastic crystal incorporated GPEs are not yet under consideration and being reported for the first time.

Experimental

Preparation of GPE films

The co-polymer, PVdF-HFP (average MW ≈ 400,000), SN, 1-ethyl-1-methylpyrrolidinium bis(trifluoromethylsulfonyl)imide (EMPTFSI), and lithium bis(trifluoromethyl-sulfonyl)imide (LiTFSI) were procured from Sigma-Aldrich. These chemicals were vacuum dried for 12 h at room temperature prior to use. The GPE films were prepared by "solution-cast" technique. Following this technique, 5 mol% (0.277 g) of OIPC, EMPTFSI, was mixed in non-ionic plastic crystal SN (1.124 g) thoroughly. The host polymer PVdF-HFP (1 g) was separately dissolved in 20 ml of acetone. The EMPTFSI/SN mixture was then added to the acetone solution of PVdF-HFP and stirred thoroughly using magnetic stirrer at room temperature for ~ 24 h, and a homogeneous solution was obtained. The ratio of EMPTFSI/SN mixture and PVdF-HFP was maintained to 80:20 (w/w). Another composition, added with lithium salt LiTFSI, was prepared following the same process, as mentioned above. The only difference was that 1-mol% LiTFSI (0.335 g) was added in EMPTFSI/SN mixture before adding in PVdF-HFP solution. The LiTFSI/EMPTFSI/SN to PVdF-HFP ratio was also maintained to 80:20 (w/w). The above mixtures were poured in glass petri-dishes, and the solvent acetone was allowed to evaporate slowly. Finally, the free-standing GPE films of thickness (0.70–0.80 mm) were obtained. Thus, the following two compositions of GPE have been employed to fabricate EDLCs:

GPE-1: (5-mol% EMPTFSI in SN):(PVdF-HFP) (80:20 w/w)

GPE-2: (1-mol% LiTFSI in EMPTFSI/SN):(PVdF-HFP) (80:20 w/w)

All the GPE films were stored in dry atmosphere to avoid moisture adsorption.

Preparation of MnO_2-nanorod-electrodes

Potassium permanganate ($KMnO_4$, 99%), manganese acetate tetrahydrate ($Mn(CH_3COO)_2 \cdot 4H_2O$, 99%), and nitric acid (HNO_3, 98%) were procured from Sigma-Aldrich and used as received. The MnO_2 powders were prepared by chemical and hydrothermal methods for comparative studies. For chemical method of preparation, 0.2 M (0.316 g) of $KMnO_4$ and 0.3 M (0.735 g) of $Mn(CH_3COO)_2 \cdot 4H_2O$ were dissolved in 35 ml of de-ionized (DI) water added with 5 ml of HNO_3. The solution was stirred overnight and kept for precipitation for about 48 h. A black colored precipitate of MnO_2 was extracted by centrifuging the solution at ~ 5000 rpm for ~ 20 min. The precipitate was first washed by ethanol and then by DI water thoroughly to remove the undesirable and excess reactants. The washing with DI water was continued till the pH of water reached to 7.0.

In the preparation of MnO_2 by hydrothermal method, the solution of the composition $KMnO_4$/$Mn(CH_3COO)_2 \cdot 4H_2O$/water/$HNO_3$, mentioned above, was transferred to a teflon-lined stainless-steel autoclave shell of 50-ml capacity. The autoclave shell was sealed and kept at ~ 140 °C for 12 h in an oven. Thereafter, it was allowed for natural cooling to room temperature. The brown colored MnO_2 was collected by centrifugation and washed thoroughly with ethanol and DI water

following the same procedure, as mentioned above for chemically prepared MnO$_2$. The MnO$_2$ samples were dried under vacuum at room temperature for 24 h. The chemically and hydrothermally prepared MnO$_2$, to be used as electrode materials in pseudocapacitors, are referred as MnO$_2$-c and MnO$_2$-h, respectively, in the rest of the text.

In order to prepare the capacitive electrodes, the MnO$_2$-c or MnO$_2$-h powder was added with conductive additive acetylene black (AB) and acetone solution of PVdF-HFP (as binder) and mixed thoroughly in agate mortar and pestle to form slurry. The weight ratio of MnO$_2$, AB, and PVdF-HFP was maintained to 80:15:5. The slurry was spread on the flexible graphite sheet (~250-μm thick, Nickunj Eximp Entp., India) and dried in vacuum at ~80 °C overnight.

Instrumentation

The electrochemical characterization of the GPE films was performed by measuring ionic conductivity and ESW. The ionic conductivity of the films was evaluated by EIS, and ESW was estimated by linear sweep voltammetry (LSV). The electrochemical analyzer (660E, CH Instruments, USA) was used for EIS and LSV measurements. The EIS measurements were carried out on the cells of the configuration SS|GPE-film|SS (SS: stainless steel foil) for the frequency range from 0.1 Hz to 100 kHz.

Morphological studies of the MnO$_2$ powders were carried out with the help of field emission scanning electron microscope (FESEM, JSM 5600, JEOL) and high-resolution transmission electron microscope (HRTEM, Tecnai G2T30, U-TWIN). The LiB$_6$ filament was employed as electron source. The working voltage range was kept at 50–100 kV. The SEM images were recorded at low vacuum after sputtering the samples with gold to prepare conducting surfaces. The samples for TEM were prepared on carbon-coated copper grid (Electron Microscopy Sciences, USA). The XRD patterns of the electrode materials were recorded using a high-resolution X-ray diffractometer (Model-D8 Discover, Bruker, USA) with CuKα radiation ($\lambda = 1.5406$ Å) in the Bragg's angle (2θ) range from 50° to 70°. Brunauer-Emmett-Teller (BET) surface area, and total pore volume of MnO$_2$ powders were measured using a surface area and pore size analyzer (model: Gemini-V, Micromeritics, Norcross, USA).

The performance characteristics of the pseudocapacitors were evaluated by using EIS, CV, and galvanostatic charge-discharge tests. The EIS studies were performed in the frequency range from 10 mHz to 100 kHz using an electrochemical analyzer mentioned above. The CV responses were also recorded with the same electrochemical analyzer. The charge-discharge tests were performed using a charge-discharge unit (BT-2000, Arbin Instruments, USA).

Results and discussions

Electrochemical properties of GPEs

Electrochemical properties of GPE films have been evaluated in terms of ionic conductivity and ESW. The electrical conductivity of pure SN at room temperature has been recorded to be ~ 1×10^{-7} S cm^{-1}, which is mainly due to the presence of impurities [66, 67]. When 80 wt% of SN is added to PVdF-HFP, the composite film shows electrical conductivity of ~ 2.2×10^{-7} S cm^{-1} at room temperature, which is also possible due to the presence of impurities. The conductivity of PVdF-HFP/EMPTFSI (20:80 *w/w*) has been found to be ~ 9.6×10^{-6} S cm^{-1} at room temperature. Upon the addition of 5 mol% of EMPTFSI in PVdF-HFP/SN, a substantial jump in conductivity has been observed by four orders of magnitude from ~ 2.2×10^{-7} to ~ 3.3×10^{-3} S cm^{-1}. This jump in conductivity is owing to the introduction of ionic mobility on adding OIPC (EMPTFSI) in PVdF-HFP network containing non-ionic plastic crystal SN. This indicates the main role of SN in enhancing the conductivity of GPE film as it helps in providing high mobility to component ions of OIPC (EMP$^+$ and TFSI$^-$) via paddle-wheel mechanism [59]. On the addition of LiTFSI to EMPTFSI/SN/PVdF-HFP, the gel polymer electrolyte (GPE-2) shows ionic conductivity of ~ 9.9×10^{-3} S cm^{-1}. This indicates substantial effect of the Li-salt addition on the ionic conductivity of the GPE; hence, it gives significant influence on the performance of the capacitor characteristics, presented in the following sections.

The ESW (i.e., working voltage range) for a typical composition of the GPE films with 5 mol% of EMPTFSI in SN has been evaluated by LSV. The LSV response was recorded on the cell:SS/GPE film/Ag (Ag is silver foil), using SS (stainless steel foil) as a working electrode and Ag as both the counter and reference electrodes. The SN-based GPE film is found to be electrochemically stable up to ~ 3.8 V versus Ag. The range of the ESW observed for the present SN/EMPTFSI-based GPE is enough for the electrochemical applications, including pseudocapacitors/supercapacitors.

## Morphological/structural and porosity analyses on MnO$_2$-electrode materials

Figure 1a–d presents the SEM and TEM images of chemically and hydrothermally prepared MnO$_2$ powders (MnO$_2$-c and MnO$_2$-h). The images indicate the 1D-nanorod structured morphology for both the materials. The SEM/TEM images of chemically prepared sample (MnO$_2$-c) show haphazardly distributed nanorods of variable thicknesses. Their thicknesses are non-uniform throughout their lengths also. In addition, substantial bulk impurities are attached to the nanorods, as distinctly evident from the TEM image (Fig. 1c). On the other hand,

the hydrothermally prepared material (MnO$_2$-h) shows relatively uniform morphology of 1D-nanorods. Bundles of uni-directional rods are observed in SEM image (Fig. 1b). As indicated in TEM images (Fig. 1d and Fig. S1), the MnO$_2$-h material possesses nanorods of uniform thicknesses throughout their lengths and the absence of bulk impurities attached to these nanorods, indicating clean morphology as compared to chemically prepared MnO$_2$-c.

Figure 1e shows the XRD patterns of MnO$_2$-c and MnO$_2$-h, recorded at room temperature. The XRD peaks of the materials have been compared with JCPDS data (No. 44-0141) and various phases of MnO$_2$, reported by Ghodbane et al. [68]. The following important points are noted from the comparison of the XRD features of MnO$_2$, prepared from two different processes:

(i)   The chemically prepared MnO$_2$-c shows the XRD peaks predominantly corresponding to crystallographic form namely octahedral molecular sieve (OMS-5) with tunnel size 4×2 Å having monoclinic system with a C2/m space group [68].

(ii) Relatively larger number of XRD peaks are observed for hydrothermally prepared MnO$_2$-h material. These peaks are indexed to pure α-MnO$_2$ phase when compared with JCPDS data (No. 44-0141). No other characteristic peaks from impurities are noted, indicating the high purity of MnO$_2$-h sample (Fig. 1e). The α-phase of MnO$_2$ basically contains double chains of edge-sharing MnO$_6$ octahedra, linked at the corners to form $(2 \times 2) + (1 \times 1)$ tunnel structures in a direction parallel to the c-axis of the tetragonal unit cell [69]. This tunneled texture is most suitable for intercalation and de-intercalation of various electrolyte cations [70, 71].

Fig. 1 SEM images of **a** MnO$_2$-c and **b** MnO$_2$-h and TEM images of **c** MnO$_2$-c and **d** MnO$_2$-h. **e** shows XRD patterns of chemically and hydrothermally derived MnO$_2$-nanorods. **f** shows N$_2$ adsorption–desorption isotherm of the MnO$_2$-c and MnO$_2$-h powders. The pore size distributions of both materials are shown in the inset of **f**
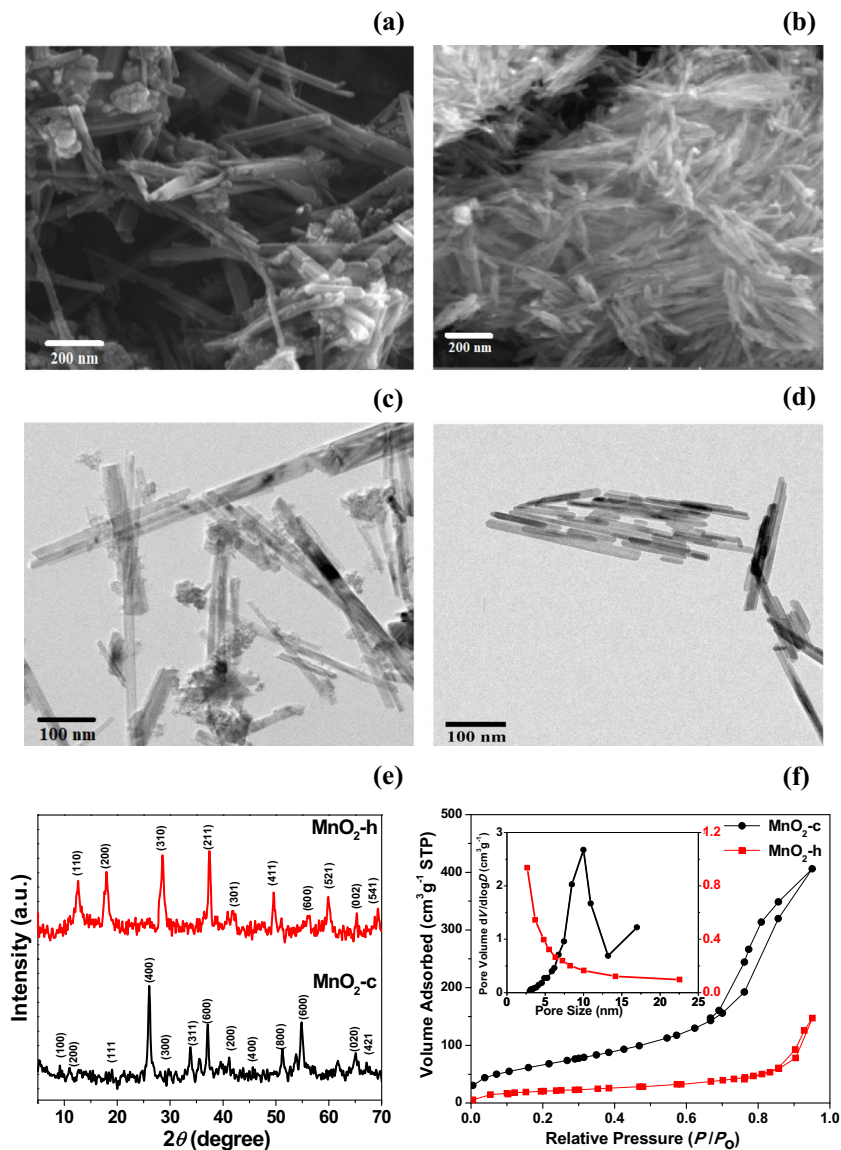
The N$_2$-adsorption–desorption isotherms of the chemically and hydrothermally prepared MnO$_2$ (MnO$_2$-c and MnO$_2$-h) nanorods are presented in Fig. 1f. The patterns show the typical type-II isotherms according to the IUPAC classification of pores. Desorption curves show distinct hysteresis loops for both the materials in the range of P/P_o from 0.65 to 0.95. The shape of the hysteresis loops suggests the nanorod-like structure of the materials [30]. The gradual increase in adsorption isotherm followed by hysteresis loop, while the desorption indicates the presence of predominantly mesoporous interiors in both the materials. The MnO$_2$-c powder shows larger adsorption of nitrogen for entire range of P/P_o; hence, larger surface area is expected as compared to that of MnO$_2$-h powder. The specific surface area of MnO$_2$-c and MnO$_2$-h was calculated using the BET equation [72] and found to be $\sim$ 241 and $\sim$ 79 m^2 g^{-1}, respectively. As previously discussed, substantial bulk impurities are attached to the nanorods of MnO$_2$-c, which appears to be the main reason of its larger surface area relative to MnO$_2$-h. On the other hand, the MnO$_2$-h powder shows substantially higher than the reported value (2.5–3 m^2 g^{-1}) for bulk MnO$_2$ structure [73, 74]. The total pore volume of MnO$_2$-c and MnO$_2$-h powders has been estimated by the Barrett-Joyner-Halenda (BJH) method and found to be $\sim$ 0.70 and $\sim$ 0.36 cm^3 g^{-1}, respectively, which are larger than the pore volume of bulk MnO$_2$, i.e., 0.65×10^{-2} cm^3 g^{-1}, reported in literature [74]. The pore size distribution has also been estimated by the BJH method, as shown in Fig. 1f (inset). This indicates that the hydrothermally prepared material (MnO$_2$-h) shows a narrow distribution of pore size around 2.75 nm. The chemically prepared MnO$_2$-c powder, on the other hand, shows larger pore distribution between $\sim$ 5 and 15 nm, with highest number of pores of size $\sim$ 10 nm. The relatively high specific surface area and pore volume and mesoporous interiors provide high accessibility of electrolyte ions for redox reactions, leading to the high pseudocapacitance of the electrode materials MnO$_2$-nanorods with respect to bulk materials.

Fabrication and electrochemical characterization of pseudocapacitors

Pseudocapacitor cells were fabricated in two-electrode geometry by the following process. Fine layer of the acetone solution of the composition of GPE-1 or GPE-2 was coated on the surface of MnO$_2$-electrodes and dried them by evaporating acetone in vacuum. To obtain the symmetric configuration of capacitor cells, two such systems were stacked over each other such that the GPE film is sandwiched between two MnO$_2$-electrodes. The following four configurations of pseudocapacitor cells, with two types of electrodes (MnO$_2$-c and MnO$_2$-h) and two compositions of GPEs (GPE-1 and GPE-2), are under investigation:

Cell-1: MnO$_2$-c/GPE-1/MnO$_2$-c
Cell-2: MnO$_2$-c/GPE-2/MnO$_2$-c
Cell-3: MnO$_2$-h/GPE-1/MnO$_2$-h
Cell-4: MnO$_2$-h/GPE-2/MnO$_2$-h

The pseudocapacitor cells were characterized using EIS, CV, and galvanostatic charge-discharge tests as discussed in the following sections.

Electrochemical impedance spectroscopy

Figure 2a–d shows EIS (Nyquist) plots for all the pseudocapacitor cells (Cell-1 to Cell-4) fabricated with chemically and hydrothermally prepared MnO$_2$-electrodes (MnO$_2$-c and MnO$_2$-h) and GPEs (with and without Li-salt). The EIS patterns indicate the capacitive nature of the electrode-electrolyte interfaces of all the cells, as reflected by the steeply rising patterns in the lower frequency range. The expanded representation of EIS plots towards the high/middle frequency region is depicted as inset of each figure (Fig. 2a–d). A semicircular spur has been observed for each cell in the high-frequency region, which represents the bulk cell resistance (R_b) and charge-transfer resistance (R_{ct}) at the interfaces of each cell, as indicated by arrows (Fig. 2a, inset). The resistance R_b represents the combination of resistances due to the electrode and electrolyte components [54, 75]. The estimated values of R_b and R_{ct} for each capacitor cell are listed in Table 1. Just after semi-circular arc, the EIS pattern of each cell shows a linear slope up to a certain frequency in the middle frequency region (Fig. 2, insets). This is the effect of Warburg impedance due to the finite diffusion limit of ion transport in electrodes on the charge-transfer processes [7, 75]. The range of the linear slope (hence, the diffusion limit of ion transport) is found to be the least in the case of Cell-4 (with MnO$_2$-h electrodes and Li-ion incorporated GPE-2).

The overall capacitance (C_o) at 10 mHz and specific capacitance (C_s) of the pseudocapacitor cells have been evaluated from the expressions: $C_o = 1 / \omega Z''$ and $C_s = 2C_o / m$, respectively, where ω is the angular frequency, Z'' is the imaginary part of impedance (Z), and m is the active mass of single electrode. The values of C_s have also been listed in Table 1 for all the cells. A comparison of Cell-3, fabricated with hydrothermally prepared MnO$_2$ (i.e., MnO$_2$-h) and GPE-1 film (without Li-salt), offers $\sim$ 1.6 times higher specific capacitance as compared to that for Cell-1 with chemically prepared MnO$_2$ (MnO$_2$-c) and the same GPE-film. Almost the same improvement in specific capacitance has been observed in Cell-4 with respect to Cell-2, when Li-salt incorporated electrolyte (i.e., GPE-2) is employed. This shows the superior capacitive performance of hydrothermally prepared MnO$_2$-h electrodes over their chemically prepared counterparts, although their specific surface area and pore volume are larger. The relatively clean and uniform morphology of hydrothermally prepared MnO$_2$-h nanorods (discussed

Fig. 2 EIS plots of pseudocapacitor cells (Cell-1 to Cell-4). Expanded representations of high-frequency regions are shown in the inset of each figure
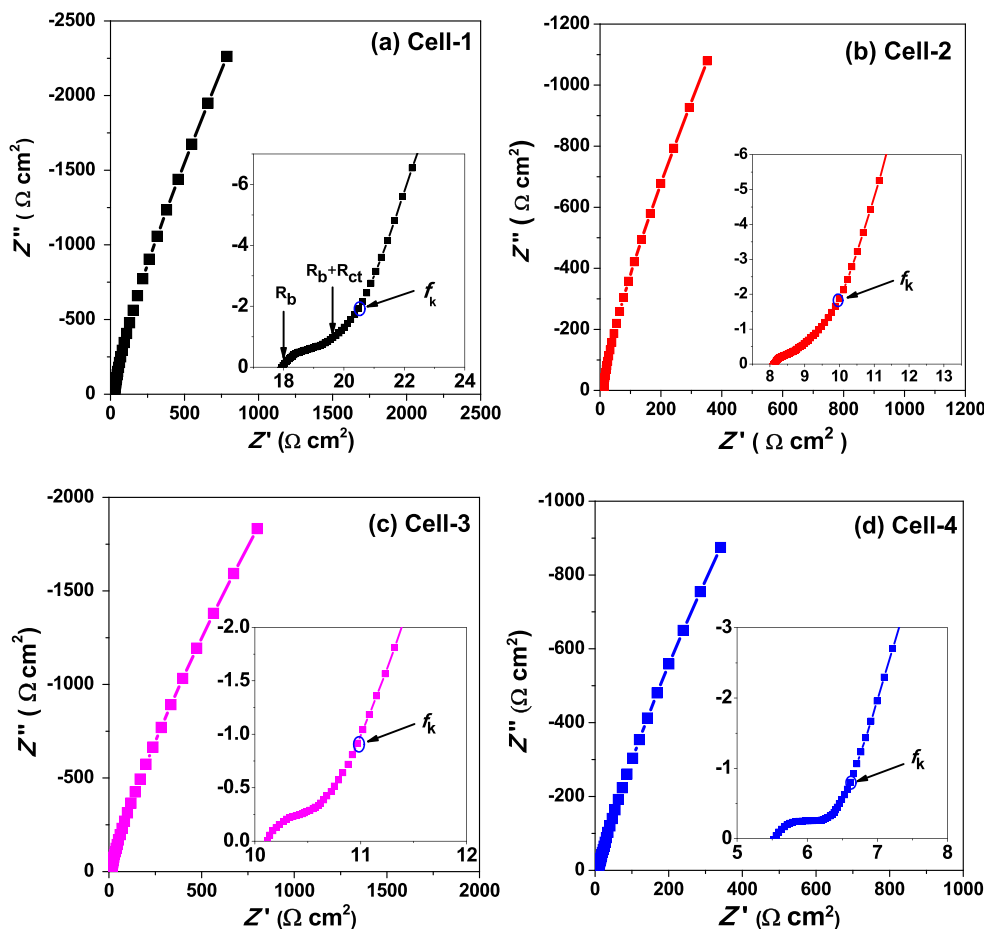
above) favors in offering better pseudocapacitive performance than chemically prepared MnO_2-c.

A further comparison of Cell-1 with Cell-2 and Cell-3 with Cell-4 refers to the effect of Li-salt incorporated GPE on the capacitive performance of the cells (Table 1). About 1.8–2.0 times enhancement in specific capacitance has been obtained when the electrolyte GPE-1 (without Li-salt) is replaced by the GPE-2 film (with Li-salt). This indicates the significant contribution of Li-ions in the pseudo-capacitive reactions via their insertion/extraction through porous MnO_2-nanorod-electrodes. It may be noted that optimum specific capacitance has been observed for the Cell-4. Synergistic effect of MnO_2-h electrodes (with clean and uniform nanorod texture, high surface area, and mesoporous character) and Li-ion containing GPE is responsible to obtain the optimum capacitive behavior of the Cell-4.

Substantial (1.8–3.6 times) reduction in the values of cell resistance (R_b) and charge-transfer resistance (R_{ct}) has been noted (Table 1), when MnO_2-c electrodes are replaced by MnO_2-h electrodes and the electrolyte GPE-1 (without Li-salt) is substituted by the Li-salt incorporated GPE-2 film. The better morphology and porosity of the MnO_2-h electrodes and Li-ion incorporation in GPE also leave significant impact on the resistive values of the capacitor cells. The reduction in the values of resistive components gives direct impact reciprocally on the specific power of the capacitors.

Comparative rate performance of the pseudocapacitor cells has also been studied from EIS analyses. Knee frequency (f_k) is one of the key parameters, which effectively determines the rate capability of the cells [54, 76]. It is the frequency below which the EIS pattern starts showing steeply rising capacitive

Table 1 Electrical parameters of the pseudocapacitor cells from EIS analysis

Capacitor Cells	R_b (Ω cm^2)	R_{ct} (Ω cm^2)	C_s (F g^{-1})	f_o (Hz)	τ_o (s)	Energy at f_o (W h kg^{-1})	Pulse power (kW kg^{-1})	Knee freq. (f_k) (Hz)
Cell-1	18.0	1.50	18–21	1.36	0.74	0.9	4.3	56
Cell-2	8.0	1.80	36–39	1.88	0.53	2.4	16	18
Cell-3	10.0	0.57	29–33	3.70	0.27	1.4	18	142
Cell-4	5.5	0.50	58–61	2.95	0.34	2.7	28	56

pattern. The Cell-3 and Cell-4 (with MnO$_2$-h electrodes) show higher f_k values with respect to Cell-1 and Cell-2 (with MnO$_2$-c electrodes) (Table 1). This indicates significantly higher rate performance of hydrothermally prepared MnO$_2$-h electrodes due to their uniform and clean morphology and higher surface area with mesoporosity as compared to those of chemically prepared electrodes (MnO$_2$-c). A comparison of Cell-1 with Cell-2 and Cell-3 with Cell-4 indicates a substantial lowering in knee frequencies (Table 1). This shows that adsorption-desorption of electrolyte ions takes place from electrode surface only in the case of GPE-1 (without Li-salt), which leads to higher rate performance of the cells. On the other hand, Li-ion intercalation/extraction occurs through MnO$_2$-electrodes when Li-salt incorporated GPE-2 is employed, which is responsible to reduce the rate performance.

Miller's approach [77] has also been adopted to determine the rate capability of the capacitor cells. According to this approach, different parameters have been evaluated from the Bode plots, i.e., the variations of Z' and Z'' versus frequency, as typically shown in Fig. 3a, b. One of the parameters is resonant frequency (f_o) at which the Bode plots of Z' and Z'' intersect each other (Fig. 3a, b) at the phase angle 45°. The

reciprocal of f_o is referred to as response time (τ_o), which is an important characteristic of a capacitor cell, also called "figure of merit." Another related parameter, namely pulse power density (P_o) of each cell, has been estimated, which is expressed as $P_o = E_o / \tau_o$, where E_o is the specific energy evaluated at the frequency f_o. The specific energy E_o has been estimated from $E_o = 1 / 2C_oV^2$, where C_o is the capacitance evaluated at f_o and V is the rated voltage range of the capacitor. The values of f_o, τ_o, E_o, and P_o are listed for each capacitor cell in Table 1. The approach of Taberna et al. [78] has also been adopted to estimate the response times of all the cells. Accordingly, the values of C' and C'' (the real and imaginary components of complex capacitance) are plotted against frequency, as shown in Fig. 3c for a typical cell (Cell-4). The resonant frequency f_o (and response time τ_o) for each cell has been found to be the same as observed from the Miller's approach. It may be noted that the specific pulse power values for Cell-2 and Cell-4 (with Li-salt) are higher as compared to those of Cell-1 and Cell-3 (without Li-salt), respectively (Table 1). The higher values of pulse power are actually not expected for Cell-2 and Cell-4 as their corresponding response times (τ_o), which are reciprocally related to pulse power, are

Fig. 3 **a** and **b** Real and imaginary parts of complex impedance Z' and Z'' versus frequency plots (i.e., Bode plots) for typical pseudocapacitor cells (Cell-2 and Cell-4), **c** real and imaginary parts of complex capacitance C' and C'' versus frequency plots for Cell-4, and **d** phase angle versus frequency plot for Cell-4
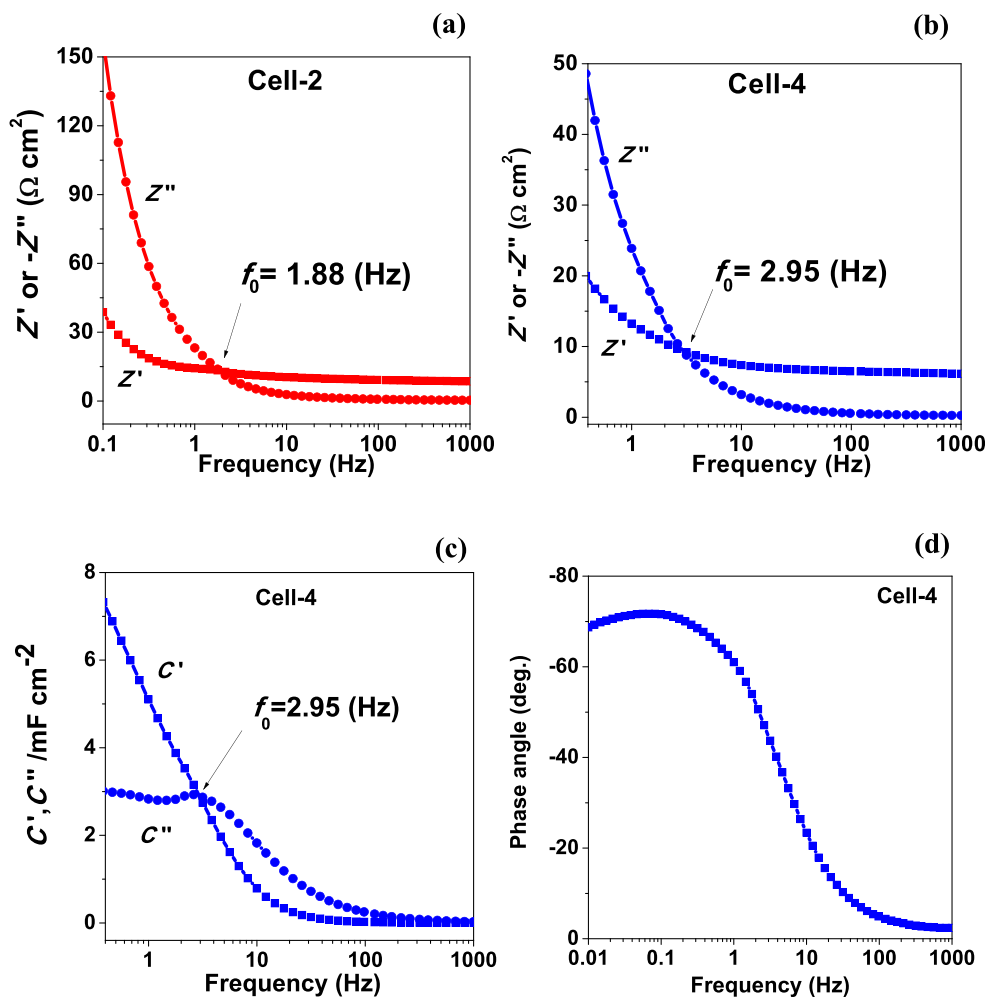
higher. However, since specific energy E_o (measured at f_o) is also high significantly due to intercalation/ extraction of Li-ions, the pulse power of these cells is observed to be higher, though the rate capability of these cells are relatively low, as discussed above.

Figure 3d depicts the phase angle variation with frequency for the optimized pseudocapacitor cell (Cell-4). The ideal capacitor cell shows the phase angle of 90° for a very wide frequency range. The capacitor cell shows phase angle ~ 70° in the lower frequency region from 0.01 to 1 Hz. This indicates the capacitive behavior of the cell for lower frequency range only, as indicated from EIS plots also (Fig. 2) presented above.

Cyclic voltammetry

The electrochemical test of all the pseudocapacitor cells (Cell-1 to Cell-4) has been performed by CV in two electrode configurations. Figure 4a shows a comparison of CV patterns of Cell-2 and Cell-4, fabricated with MnO_2-c and MnO_2-h electrodes, respectively, employing the same electrolyte (Li-salt incorporated GPE-2). This indicates that the hydrothermally derived MnO_2-nanorod-electrodes offer higher voltammetric current (hence, higher specific capacitance) as compared to that of nanorod electrodes derived chemically. The MnO_2-h electrodes show similar voltammetric behavior with respect to MnO_2-c electrodes with the electrolyte GPE-1 also, which has no Li-salt (Fig. S2). This is owing to the clean and uniform morphology of MnO_2-h electrodes along with their high

surface area and mesoporous interiors, which allow facile transport of electrolyte ions through them, as discussed earlier.

To see the effect of Li-salt addition in GPE on the performance of capacitor cells, CV pattern of Cell-4 (with Li-salt) has been compared to that of Cell-3 (without Li-salt) (Fig. 4b). A significantly higher voltammetric current (hence higher specific capacitance) has been obtained when Li-salt incorporated GPE (GPE-2) has been employed in the capacitor cell with respect to the cell containing GPE-1 (without Li-salt) (Fig. 4b). This indicates the insertion/extraction of Li-ions through MnO_2-electrodes, responsible to the improvement in the capacitance of the cell. Distinct quasi-reversible humps, overlapped on the voltammogram of Cell-4, are also present as shown by arrows in (Fig. 4b), which further confirm the insertion/extraction of Li-ions. Such quasi-reversible humps, indicating insertion/extraction of Li-ions through MnO_2-electrodes, are distinctly seen in CV responses of Cell-2 and Cell-4 recorded at lower scan rate (2 mV s^{-1}), as shown in Fig. S3. As discussed earlier, the hydrothermally derived MnO_2-h nanorods are in α-phase (i.e., α-MnO_2), containing tunneled structure, through which insertion/extraction of Li-ions is possible. It may be noted that such feature is not observed for Cell-3 containing GPE without Li-salt (Fig. 4b). Similar conclusion has been drawn from the EIS studies, discussed above.

Figure 4c depicts the CV responses of a typical cell (Cell-4 with MnO_2-h nanorod-electrodes and Li-ions incorporated GPE-2 film) for different scan rates. The scan rate dependent CV responses for other cells are shown in Fig. S4 for comparison. Almost rectangular box-like voltammograms (indicating

Fig. 4 Comparative CV responses of capacitor cells **a** with MnO_2-c and MnO_2-h electrodes (Cell-2 and Cell-4, respectively) and Li-salt containing electrolyte GPE-2 and **b** with different electrolytes GPE-1 (without Li-salt) and GPE-2 (with Li-salt) sandwiched between MnO_2-h electrodes, recorded at scan rate 10 mV s^{-1}. **c** shows CV patterns of Cell-4 at different scan rates, **d** shows scan rate dependence of specific capacitance of the cells (Cell-1 to Cell-4)
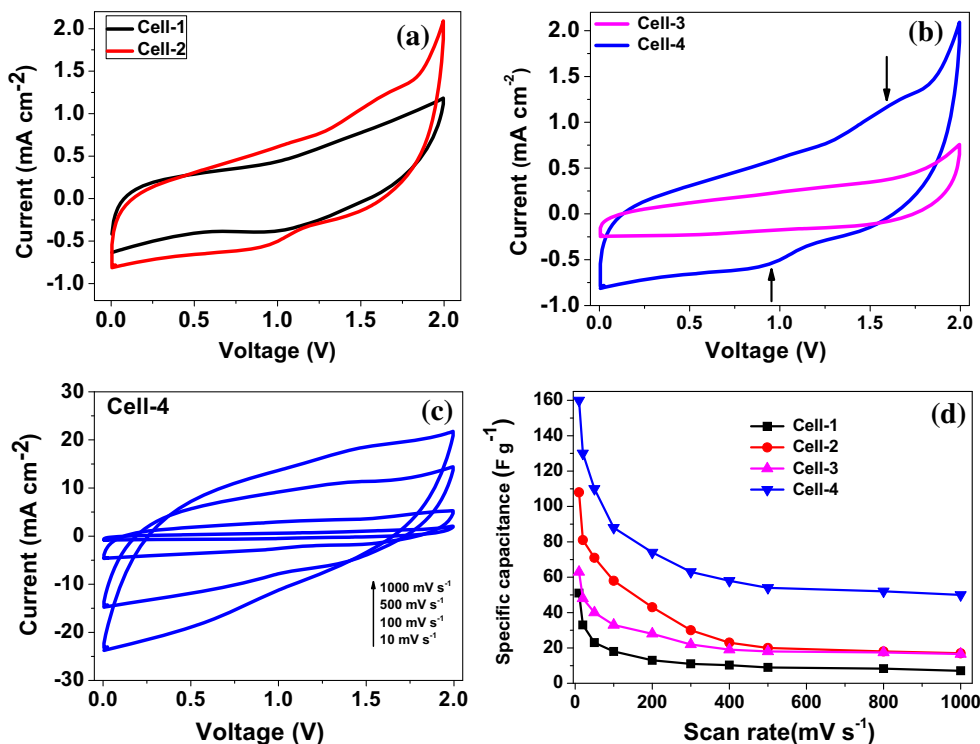
pseudocapacitive nature) of Cell-4 are observed up to the scan rate of 1000 mV s^{-1} (Fig. 4c). This confirms the high rate performance of Cell-4, as discussed in EIS studies also, presented earlier. The slightly tilted rectangular CV-responses are observed for higher scan rates, which are owing to the presence of significant resistive component/ESR of the cell. The CV patterns are substantially deviated from rectangular shapes for Cell-2 (chemically derived MnO$_2$-c electrodes) from 0 to 0.75 V at higher scan rates, as shown in Fig. S4a. Such feature is not seen for Cell-4, which further indicates the superior capacitive and rate performance of MnO$_2$-h electrodes. Figure 4d depicts the variation of specific capacitance as function of scan rates for all the cells. The specific capacitance (C_s) values have been evaluated from CV patterns using the expression: $C_s = 2i / (m \times s)$, where i is the voltammetric current, m is the mass of active material (MnO$_2$) in single electrode, and s is the scan rate. Usual patterns of variation, i.e., fast initial decrease in specific capacitance (C_s) followed by its almost stable values with respect to scan rates have been observed for all the cells. The lowest values of C_s have been observed for the scan rates from 0.5 to 1000 mV s^{-1} for the Cell-1 (with chemically derived MnO$_2$-c nanorod-electrodes and electrolyte GPE-1 without Li-salt). On the other hand, Cell-4 (with hydrothermally-derived MnO$_2$-h-nanorod-electrodes and electrolyte GPE-2 with Li-salt) shows the highest capacitance with respect to other cells for each scan rate in the present studies. The capacitance of Cell-4 is the highest among all the cells even at the scan rate of 1000 mV s^{-1}. This further indicates the high rate performance of Cell-4.

Charge-discharge analyses

The comparative performance characteristics of the capacitor cells based on galvanostatic charge-discharge tests have been depicted in Fig. 5a–f. The charge-discharge patterns of the Cell-2 with chemically derived MnO$_2$ (MnO$_2$-c) and Cell-4 with hydrothermally derived MnO$_2$ (MnO$_2$-h), both with Li-ion containing GPE-2 films, have been recorded at constant current 1.0 mA cm^{-2} (1.4 A g^{-1}) with gradually increasing charging voltage limits (Fig. 5a, b). Both the cells have been charged up to 2.0 V. A comparison indicates that the initial sudden drops while discharging the cells, which are directly proportional to equivalent series resistance (ESR), are found to be significantly large for Cell-2 as compared to Cell-4. This indicates that the chemically derived MnO$_2$-c electrodes are more resistive relative to the hydrothermally derived MnO$_2$-h electrodes. Further, based on this study, the cells with MnO$_2$-h electrodes have been decided to charge up to 2.0 V, while the cells employing MnO$_2$-c electrodes up to 1.8 V.

Figure 5c, d shows the charge-discharge patterns of the cells with two different electrolyte films, the GPE-1 without Li-salt and GPE-2 with Li-salt, and the role of Li-ions containing GPE has been distinctly observed. From these patterns, the parameters, namely specific discharge capacitance (C_d) and ESR, have been estimated for all the cells (Cell-1 to Cell-4). The values of C_d were evaluated from the linear part of discharge characteristics using the expression $C_d = 2i\Delta t / (m\Delta V)$, where i is the discharge current, Δt is the discharge-time interval corresponding to the voltage range, ΔV (excluding initial voltage drop) is the mass of active material (MnO$_2$-c or MnO$_2$-h) in single electrode. The ESR of each cell was evaluated from the initial sudden voltage drop observed in discharge profile, which is an ohmic drop across ESR of the cell. The specific discharge capacitance (C_d) and ESR of each cell are listed in Table 2. A comparison of discharge capacitance (C_d) of Cell-1 with Cell-2, and Cell-3 with Cell-4 indicates the distinct effect of Li-ion incorporated GPE employed in pseudocapacitor cells. The values of C_d have been enhanced by almost double when GPE-1 films (without Li-salt) are substituted by GPE-2 (with Li-salt) in the capacitor cells (Table 2). A comparative performance also indicates the 2.0–2.4 times enhancement in C_d values of the cells when MnO$_2$-h (hydrothermally derived) electrodes are employed in pseudocapacitor cells in place of MnO$_2$-c (chemically derived) electrodes (Table 2). The substitution of Li-ion containing GPE-2 also affects ESR values of the cells (Table 2). A substantial (~ 2.6 times) lowering in ESR has been observed in Cell-4 (with Li-ions incorporated electrolyte, GPE-2) compared to Cell-3 (with electrolyte without Li-ions, GPE-1). The enhancement in specific capacitance and lowering in resistive components were also observed in EIS studies on the pseudocapacitor cells, discussed above.

As discussed earlier, the improvement in specific capacitance and lowering in ESR is directly related to improvement in specific energy and specific power, respectively. The specific energy (E) and maximum specific power (P_{max}) of all the cells have been evaluated using the expressions: $E = {}^1/_8 C_d V^2$ and $P_{max} = {}^{V^2}/_{(8m \times ESR)}$, respectively, where V is the rated voltage of the cells and m is the active mass of the single electrode. Values of E and P_{max} for all the cells have also been listed in Table 2. Significant improvement in specific energy and power has been noted (Table 2) mainly due to cleaner morphology of MnO$_2$-h electrodes as compared to MnO$_2$-c electrodes and use of Li-salt incorporated GPE-2 films in place of GPE-1 film (without Li-salt). The Cell-4, configured with Li-salt containing GPE-2 film sandwiched between two symmetrical MnO$_2$-h electrodes, offers optimum specific capacitance, energy, and power. This further confirms the synergistic effect of clean morphology of MnO$_2$-electrodes and Li-ions incorporated GPE-2 film.

The specific capacitance, energy, and power of the present solid-state pseudocapacitor cell are found to be comparable to or even higher than the MnO$_2$-based capacitors, reported by few workers, as given in Table 3. It may be noted that a very few solid-state pseudocapacitors are reported based on MnO$_2$-

Fig. 5 **a** and **b** Galvanostatic charge-discharge curves for pseudocapacitor cells (Cell-2 and Cell-4) for different voltage limits at constant current of 1.0 mA cm^{-2} (1.4 A g^{-1}), **c** and **d** comparative charge–discharge curves for different cells recorded at 1.0 mA cm^{-2}, **e** charge–discharge curves of Cell-4 at different current densities, and **f** variation of discharge specific capacitance of capacitor cells (Cell-3 and Cell-4) as a function of current density
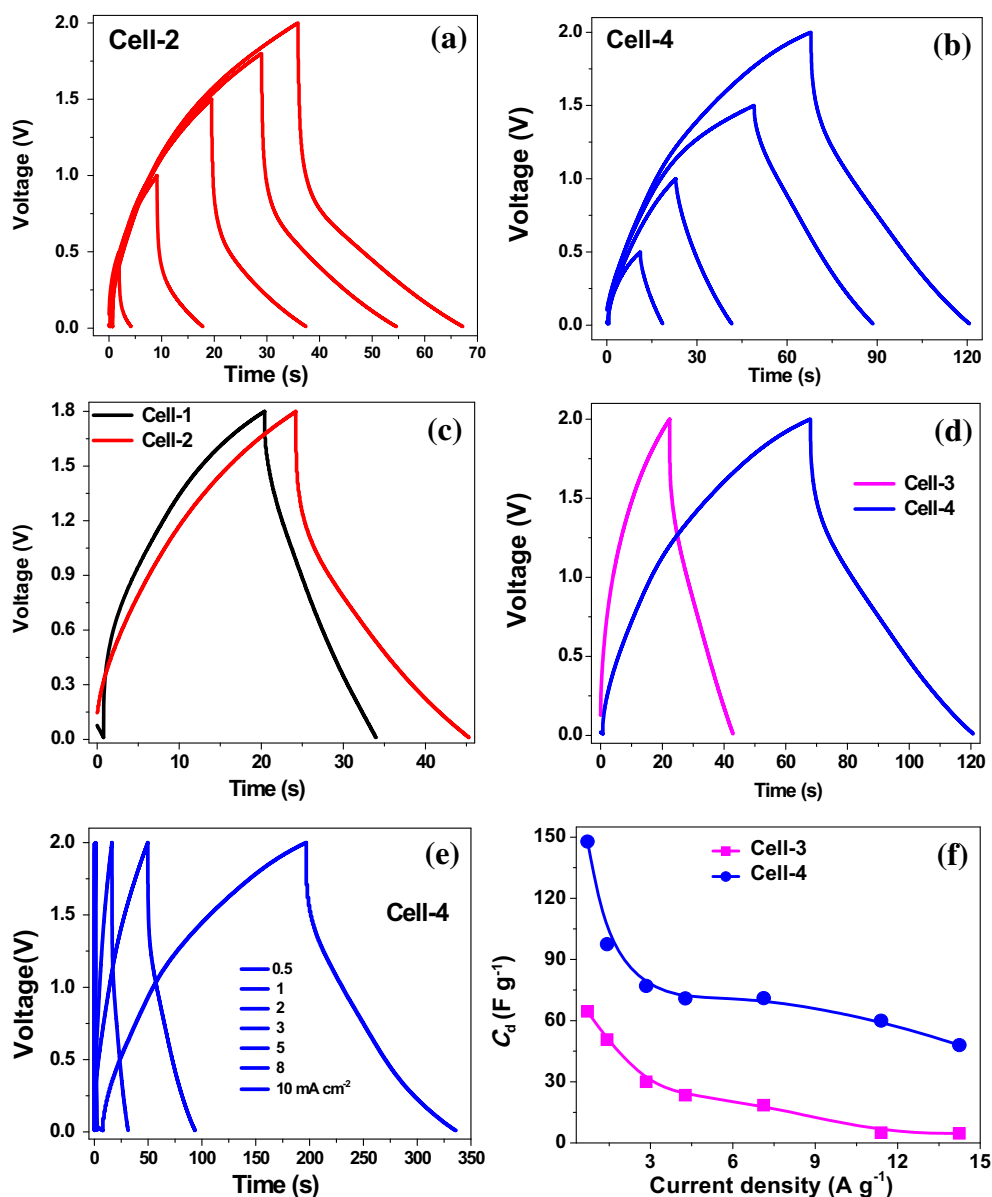
electrodes with GPEs (Table 3). For example, Chodankar et al. [64] reported capacitor of MnO$_2$ nanoflakes as electrodes fabricated with GPE (PVP-LiClO$_4$), which offers specific capacitance, energy, and power of ∼ 134 F g^{-1}, ∼ 23 W h kg^{-1}, and ∼ 1.9 W kg^{-1}, respectively. The same GPE has been used to form capacitor with MnO$_2$ thin film electrodes, prepared from chemical bath deposition, which gives lower value of capacitance and energy (∼ 112 F g^{-1} and ∼ 15 W h kg^{-1}, and slightly higher value of power (∼ 3.8 W kg^{-1}) [81]. The MnO$_2$-electrodes of nanoflake morphology has been used to fabricate capacitor with another GPE PVA-H$_3$PO$_4$, showing low value of capacitance (2.3 mF cm^{-2}) [82]. Another solid capacitor with ionic liquid based GPE (BMIBF$_4$/PVdF-HFP) has been reported with electrochemically deposited MnO$_2$ thin film electrodes, which also shows lower value of capacitance,

energy, and power (Table 3) [83]. In another study [65], the aqueous GPEs, namely PAAK:KCl:H$_2$O and PAAK-co-PAAM:KCl:H$_2$O have been employed to fabricate solid-state capacitors with chemically prepared hydrous MnO$_2$-electrodes. These devices offer relatively high capacitance (235–253 F g^{-1}); however, their energy and power densities are not reported. The present optimized pseudocapacitor cell employing plastic crystal-based electrolyte and hydrothermally prepared MnO$_2$-nanorod-electrodes (Cell-4) offers high specific capacitance and energy (Table 3). Particularly, the capacitor shows high specific power (∼ 32.6 kW kg^{-1}), which is due to high rate capability of the cell, discussed earlier.

The charge-discharge profiles of a typical pseudocapacitor (Cell-4) at different current densities are shown in Fig. 5e. Figure 5f depicts the variation of specific discharge

Table 2 Typical charge–discharge characteristics of pseudocapacitor cells at a constant current density 1.0 mA cm^{-2} (1.4 A g^{-1})

EDLC cells	ESR (Ω cm^2)	"C_d" (F g^{-1})	Specific energy "E" (W h kg^{-1})	Specific power "P_{max}" (kW kg^{-1})
Cell-1	47.0	22–24	2.5	11.0
Cell-2	38.0	50–52	7.1	16.9
Cell-3	62.5	52–55	7.1	12.5
Cell-4	24.0	98–101	13.7	32.6

capacitance (C_d) as a function of current densities, which also gives indication of the rate performance of the capacitor cells. It has been noted that the capacitance C_d reduces steeply for Cell-3 (with GPE-1 without Li-salt), indicating slow kinetics of the adsorption-desorption of the relatively larger size electrolyte ions (component ions of OIPC EMPTFSI) at the interfaces. The Cell-4 (with GPE-2 with Li-salt), on the other hand, shows almost stable performance (i.e., a gradual decrease in specific capacitance for higher current densities) after its initial fast decrease. This is due to possible fast intercalation/ extraction of Li-ions via mesoporous MnO$_2$-h nanorod-electrodes at the interfaces even up to higher current densities.

Figure 6a shows a comparative Ragone plots for Cell-3 and Cell-4 fabricated with hydrothermally derived MnO$_2$-h electrodes, employing electrolytes GPE-1 (without Li-salt) and GPE-2 (with Li-salts) films, respectively. In Ragone plots, the specific energy, E (evaluated at different current densities), is plotted against effective specific power (P_{eff}), evaluated from the expression: $P_{eff} = E / t$, where t is the discharge time (in s) of the cells. The Cell-3 shows a drastic fall in specific energy with respect to increasing power; on the other hand, Cell-4 shows stable performance, i.e., very less fading in specific energy has been observed with increasing effective power. The Cell-4 (with Li-salt) offers higher specific energy compared to Cell-3 (without Li-salt), e.g., ~ 20.5 W h kg^{-1} at power ~ 540 W kg^{-1}, and 6.7 W h kg^{-1} at power ~ 15.7 kW kg^{-1}. This further indicates an effective role of Li-ions in the performance of pseudocapacitor cell providing better switching behavior at the electrode-electrolyte interfaces.

The charge-discharge reversibility test, i.e., the cyclic performance measurement of the optimized capacitor cell (Cell-4) has been recorded for 3300 charge-discharge cycles at a constant current of 1.0 mA cm^{-2} (1.4 A g^{-1}). Figure 6b shows the variation of specific capacitance of the Cell-4 as a function of charge-discharge cycles. About 17% fading in specific capacitance has been observed for about 100 cycles initially; thereafter, the cell shows almost stable performance showing gradual decrease in capacitance values with respect to charge-discharge cycles. The initial fading is related to the possible formation of irreversible product like Mn(OH)$_2$ due to the possible adsorption of OH$^-$ groups from atmosphere on to the MnO$_2$-electrode surface.

Table 3 Performance characteristics of pseudocapacitors based on MnO$_2$-electrodes having different morphologies

Morphology/type	Synthesis techniques	Electrolyte used	Specific capacitance (F g^{-1})	Specific energy W h kg^{-1}	Specific power kW kg^{-1}	Ref.
Nanorods	Hydrothermal	1 M Na$_2$SO$_4$ (aqueous electrolyte)	118 (5 mV s^{-1})	⋯	⋯	[29]
Hollow spheres	Hydrothermal	1 M Na$_2$SO$_4$ (aq. solution)	167, 147, 124 (2.5, 5, 10 mA)	⋯	⋯	[71]
Nanowire	Chemical precipitation	1 M Na$_2$SO$_4$ (aq. solution)	121 (100 mV s^{-1})	⋯	⋯	[79]
Nanospheres (without IL)	Sol-gel method	5% IL (Aliquat HTA-1)	321 (1 mV s^{-1})	69	0.753	[80]
Nanorods (with IL)			428 (1 mV s^{-1})			
Nanoflakes	Chemical bath deposition (CBD)	PVP-LiClO$_4$	134 (100 mV s^{-1})	23	1.9	[64]
Thin film	Chemical bath deposition (CBD)	PVP-LiClO$_4$	112 (100 mV s^{-1})	15	3.8	[81]
Hydrous	Chemical	PAAK:KCl:H$_2$O (PAAK-co-PAAM:KCl:H$_2$O)	253 (4 mV s^{-1}) 235 (4 mV s^{-1})	⋯	⋯	[65]
Thin film	Pulsed electrochemical deposition	(BMIBF$_4$/PVdF-HFP)	36.68	1.27	0.292	[82]
Nanoflake	Hydrothermal	PVA/H$_3$PO$_4$	2.3 mF cm^{-2} (0.025 mA cm^{-2})	⋯	⋯	[83]
Nanorods	Hydrothermal	PVdF-HFP:EMPTFSI/SN/LiTFSI	98–101 (1.4 A g^{-1})	13.7	32.6	Present work

Aliquat-HTA-1: bis(diethylamino)-N-N-diethylmethaniminium chloride, PVP: polyvinyl pyrrolidone, PVA: poly(vinyl alcohol), PAAK: potassium polyacrylate, PAAM: polyacrylamide, BMIBF$_4$: 1-butyl-3-methylimidazolium tetrafluoroborate
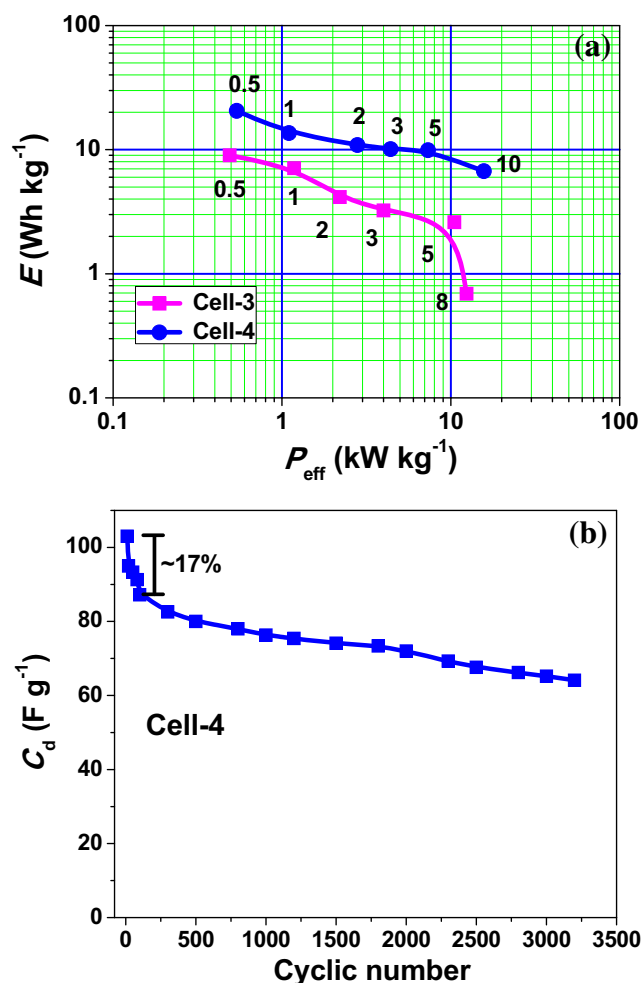
Fig. 6 a Ragone plots for capacitor cells (Cell-3 and Cell-4); numbers marked on curves are current densities for charge-discharge in mA cm^{-2} and **b** specific discharge capacitance of a typical cell (Cell-4) as a function of charge-discharge cycles

Formation of another product LiOH is also expected, in the present case, owing to the reaction between electrolyte ions (Li$^+$) and adsorbed OH$^-$ groups on the electrode surface. Such products reduce the reactive sites at the surface of electrodes [84], responsible for capacitance fading. The stable cyclic performance is also associated with the uniform nanorod morphology and mesoporous character of MnO$_2$-h electrodes, through which facile and fast pseudocapacitive reaction(s) take place with electrolyte ions including Li$^+$ ions.

Conclusions

Supercapacitive performance of MnO$_2$-nanorod-electrodes, prepared from chemical and hydrothermal processes, has been tested on PVdF-HFP-based GPE films incorporated with nonionic and ionic plastic crystals, SN and EMPTFSI, respectively. The uniform and cleaner nanorod morphology has been observed for hydrothermally-prepared material (MnO$_2$-h) as

compared to the chemically prepared MnO$_2$ (MnO$_2$-c), as observed from SEM/TEM studies. The XRD studies indicate α-phase, tunneled structure of the MnO$_2$-h electrode material. The hydrothermally prepared MnO$_2$-h nanorod material also possesses large specific surface area (~ 79 m^2 g^{-1}) with mesoporous interiors. These characteristics show the superiority of hydrothermally prepared MnO$_2$-h as capacitive electrode material over the chemically-prepared MnO$_2$-c electrodes. Further, the comparative performance has been studied on the pseudocapacitors comprising GPEs, with and without Li-salt (LiTFSI), to test the effect of Li-ions on their capacitive characteristics. On the basis of EIS, CV, and galvanostatic charge-discharge studies, the following conclusions have been drawn:

(1) Optimum values of specific capacitance, specific energy, and maximum specific power are observed for the capacitor cell with hydrothermally prepared MnO$_2$-h-nanorod-electrodes and LiTFSI containing electrolyte (GPE-2): 98–101 F g^{-1}, ~ 13.7 W h kg^{-1}, and ~ 32.6 kW kg^{-1}, respectively, evaluated from charge-discharge studies.

(2) Synergistic effect of clean and uniform morphology of MnO$_2$-h nanorod-electrodes and facile intercalation/extraction of Li-ions through them (in addition to the adsorption-desorption of the component ions of OIPC, EMPTFSI) is responsible to obtain high-performance supercapacitive parameters of the cell, mentioned above.

(3) The MnO$_2$-h nanorod-electrodes also show higher rate performance with both the electrolytes (with and without Li-salt) as determined in terms of knee frequency and response time (from EIS studies) and CV responses up to high scan rate of 1000 mV s^{-1}. High rate capability is directly related to high specific power, as observed in the present pseudocapacitor cells.

(4) The pseudocapacitor cell with optimized MnO$_2$-h electrodes show better charge–discharge stability for the current density up to 14.2 A g^{-1}, as compared to the capacitor with electrolyte without Li-salt (GPE-1). This is owing to fast intercalation/extraction of Li-ions through mesoporous MnO$_2$-h electrodes at the interfaces.

(5) The MnO$_2$-h-nanorod-electrodes show better performance with Li-salt containing electrolyte GPE-2, as observed in Ragone plots also, when compared with the capacitor cell containing electrolyte without Li-salt.

(6) The optimized capacitor cell offers almost stable cyclic performance up to ~ 3300 charge-discharge cycles with $\sim 17\%$ fading only in specific capacitance for about 100 initial cycles.

References

1. Beguin F, Frackowiak E (2013) Supercapacitors, materials, systems and applications. Wiley-VCH Verlag, Weinheim

2. Stevenson KJ (2012) The origin, development, and future of the lithium-ion battery. J Solid State Electrochem 16(6):2017–2018

3. Pistoia G (ed) (2014) Lithium ion batteries, advances and applications. Elsevier, Poland

4. Simon P, Brousse T, Favier F (2017) Supercapacitors based on carbon or pseudocapacitive materials, Hoboken, Wiley

5. González A, Goikolea E, Barrena JA, Mysyk R (2016) Review on supercapacitors: technologies and materials. Renew Sust Energ Rev 58:1189–1206

6. Hashmi SA (2014) Supercapacitor: an emerging power source. Natl Acad Sci Lett 27:27–46

7. Conway BE (1999) Electrochemical capacitors: scientific fundamentals and technological applications. Kluwer Academic/Plenum, New York

8. Yuan C, Wu HB, Xie Y, Lou XW (2014) Mixed transition-metal oxides: design, synthesis, and energy-related applications. Angew Chem Int Ed 53(6):1488–1504

9. Li Q, Zheng S, Xu Y, Xue H, Pang H (2018) Ruthenium based materials as electrode materials for supercapacitors. Chem Eng J 333:505–518

10. Kate RS, Khalate SA, Deokate RJ (2018) Overview of nanostructured metal oxides and pure nickel oxide (NiO) electrodes for supercapacitors: a review. J Alloys Compd 734:89–111

11. Tang N, Wang W, You H, Zhai Z, Hilario J, Zeng L, Zhang L (2018) Morphology tuning of porous CoO nanowall towards enhanced electrochemical performance as supercapacitors electrodes. Catal Today. https://doi.org/10.1016/j.cattod.2018.03.024

12. Jang GS, Ameen S, Akhtar MS, Shin HS (2018) Cobalt oxide nanocubes as electrode material for the performance evaluation of electrochemical supercapacitor. Ceram Int 44(1):588–595

13. Barik R, Devi N, Nandi D, Siwal S, Gosh SK, Mallick K (2017) Multifunctional performance of nanocrystalline tin oxide. J Alloys Compd 732:201–207

14. Arhin DD, Nuamah RA, Jain PK, Obada DO, Yaya A (2018) Nanostructured stannic oxide: synthesis and characterization for potential energy storage applications. Results Phys 9:1391–1402

15. Saha S, Samanta P, Kuila T (2018) A review on the heterostructure nanomaterials for supercapacitor application. J Energy Storage 17:181–202

16. Huang M, Li F, Dong F, Zhang YX, Zhang LL (2015) MnO_2-based nanostructures for high-performance supercapacitors. J Mater Chem A 3(43):21380–21423

17. Xie K, Li J, Lai Y, Lu W, Zhang Z, Liu Y, Zhou L, Huang H (2011) Highly ordered iron oxide nanotube arrays as electrodes for electrochemical energy storage. Electrochem Commun 13(6):657–660

18. Hashmi SA, Upadhyaya HM (2002) MnO_2-polypyrrole conducting polymer composite electrodes for electrochemical redox supercapacitors. Ionics 8(3-4):272–277

19. Kim H, Popov BN (2003) Synthesis and characterization of MnO_2-based mixed oxides as supercapacitors. J Electrochem Soc 150(3):D56–D62

20. Jeong YU, Manthiram A (2002) Nanocrystalline manganese oxides for electrochemical capacitors with neutral electrolytes. J Electrochem Soc 149(11):A1419–A1422

21. Toupin M, Brousse T, Bélanger D (2002) Influence of microstructure on the charge storage properties of chemically synthesized manganese dioxide. Chem Mater 14(9):3946–3952

22. Toupin M, Brousse T, Bélanger D (2004) Charge storage mechanism of MnO_2 electrode used in aqueous electrochemical capacitor. Chem Mater 16(16):3184–3190

23. Reddy RN, Reddy RG (2003) Sol–gel MnO_2 as an electrode material for electrochemical capacitors. J Power Sources 124(1):330–337

24. Pang S-C, Anderson MA (2000) Novel electrode materials for electrochemical capacitors: part II. Material characterization of sol-gel-derived and electrodeposited manganese dioxide thin films. J Mater Res 15(10):2096–2106

25. Mardi S, Moradlou O, Moshfegh AZ (2018) Fabrication and the electrochemical activation of network-like MnO_2 nanoflakes as a flexible and large-area supercapacitor electrode. J Solid State Electrochem 22(11):3507–3514

26. Lee HY, Goodenough JB (1999) Supercapacitor behavior with KCl electrolyte. J Solid State Chem 144(1):220–223

27. Brousse T, Toupin M, Dugas R, Athouël L, Crosnier O, Bélanger D (2006) Crystalline MnO_2 as possible alternatives to amorphous compounds in electrochemical supercapacitors. J Electrochem Soc 153(12):A2171–A2180

28. Li Z, Liu Z, Li B, Li D, Li Q, Wang H (2014) MnO_2 nanosilks self-assembled micropowders: facile one-step hydrothermal synthesis and their application as supercapacitor electrodes. J Taiwan Inst Chem Eng 45(6):2995–2999

29. Subramanian V, Zhu H, Vajtai R, Ajayan PM, Wei B (2005) Hydrothermal synthesis and pseudocapacitance properties of MnO_2 nanostructures. J Phys Chem B 109(43):20207–20214

30. Xu M, Kong L, Zhou W, Li H (2007) Hydrothermal synthesis and pseudocapacitance properties of α-MnO_2 hollow spheres and hollow urchins. J Phys Chem C 111(51):19141–19147

31. Tsuda M, Arai H, Nemoto Y, Sakurai Y (2003) Electrode performance of sodium and lithium-type romanechite. J Electrochem Soc 150(6):A659–A664

32. Wang X, Li Y (2002) Selected-control hydrothermal synthesis of α- and β-MnO_2 single crystal nanowires. J Am Chem Soc 124(12):2880–2881

33. Gao Y, Wang Z, Wan J, Zou G, Qian Y (2005) A facile route to synthesize uniform single-crystalline α-MnO_2 nanowires. J Cryst Growth 279(3-4):415–419

34. Liu Y, Zhang M, Zhang J, Qian Y (2006) A simple method of fabricating large-area α-MnO_2 nanowires and nanorods. J Solid State Chem 179(6):1757–1761

35. Sugantha M, Ramakrishnan PA, Hermann AM, Warmsingh CP, Ginley DS (2003) Nanostructured MnO_2 for Li-batteries. Int J Hydrog Energy 28(6):597–600

36. Thackeray MM (1997) Manganese oxides for lithium batteries. Prog Solid State Chem 25(1-2):1–71

37. Hill LI, Verbaere A, Guyomard D (2003) MnO_2 (α-, β-, γ-) compounds prepared by hydrothermal-electrochemical synthesis: characterization, morphology and lithium insertion behavior. J Power Sources 119:226–231

38. Strobel P, Thiery F, Darie C, Proux O, Ibarra-Palos A, Bacia M, Soupart JB (2005) Structural and electrochemical properties of new nanospherical manganese oxides for lithium batteries. J Mater Chem 15(45):4799–4808

39. Cheng F, Zhao J, Song W, Li C, Ma H, Chen J, Shen P (2006) Facile controlled synthesis of MnO_2 nanostructures of novel shapes and their application in batteries. Inorg Chem 45(5):2038–2044

40. Tang Y, Zheng S, Xu Y, Xiao X, Xue H, Pang H (2018) Advanced batteries based on manganese dioxide and its composites. Energy Storage Mater 12:284–309

41. Espinal L, Suib SL, Rusling JF (2004) Electrochemical catalysis of styrene epoxidation with films of MnO_2 nanoparticles and H_2O_2. J Am Chem Soc 126(24):7676–7682

605

42. Xi Y, Reed C, Lee YK, Oyama ST (2005) Acetone oxidation using ozone on manganese oxide catalysts. J Phys Chem B 109(37): 17587–17596

43. Feng Q, Kanoh H, Miyai Y, Ooi K (1995) Alkali metal ions insertion/extraction reactions with hollandite-type manganese oxide in the aqueous phase. Chem Mater 7(1):148–153

44. Liao MY, Lin JM, Wang JH, Yang CT, Chou TL, Mok BH, Chong NS, Tang HY (2003) Electrochemical synthesis of α-MnO₂ octahedral molcular sieve. Electrochem Commun 5(4):312–316

45. Li Q, Olson JB, Penner RM (2004) Nanocrystalline α-MnO₂ nanowires by electrochemical step-edge decoration. Chem Mater 16(18):3402–3405

46. Cheng X, Pan J, Zhao Y, Liao M, Peng H (2018) Gel-polymer electrolytes for electrochemical energy storage. Adv Energy Mater 8:1702184

47. Zhong C, Deng Y, Hu W, Qiao J, Zhang L, Zhang J (2015) A review of electrolyte materials and compositions for electrochemical supercapacitors. Chem Soc Rev 44(21):7484–7539

48. Xu M-W, Bao S-J (2011) Nanostructured MnO₂ for electrochemical capacitor. In: Carbone R (ed) Energy storage in the emerging era of smart grids. InTech Europe, Croatia, pp 251–278

49. Qunting Q, Zhang P, Wang B, Chen Y, Tian S, Wu Y, Holze R (2009) Electrochemical performance of MnO₂ nanorods in neutral aqueous electrolytes as a cathode for asymmetric supercapacitors. J Phys Chem C 113:14020–14027

50. Zhong C, Deng Y, Hu W, Sun D, Han X, Qiao J, Zhang J (2016) Electrolytes for electrochemical supercapacitors. CRC Press, Boca Raton

51. Pal P, Ghosh A (2018) Highly efficient gel polymer electrolytes for all solid-state electrochemical charge storage devices. Electrochim Acta 278:137–148

52. Harankahawa N, Perera K, Vidanapathirana K (2017) Use of gel polymer electrolytes to integrate photoelectric conversion and energy storage. J Energy Storage 13:96–102

53. Fan L-Z, Hu Y-S, Bhattacharyya AJ, Maier J (2007) Succinonitrile as a versatile additive for polymer electrolytes. Adv Funct Mater 17(15):2800–2807

54. Suleman M, Kumar Y, Hashmi SA (2013) Structural and electrochemical properties of succinonitrile-based gel polymer electrolytes: role of ionic liquid addition. J Phys Chem B 117(24):7436–7443

55. Singh MK, Suleman M, Kumar Y, Hashmi SA (2015) A novel configuration of electrical double layer capacitor with plastic crystal-based gel polymer electrolyte and graphene nano-platelets as electrodes: a high rate performance. Energy 80:465–473

56. Sharma J, Hashmi SA (2013) Magnesium ion transport in poly (ethylene oxide)-based polymer electrolyte containing plastic-crystalline succinonitrile. J Solid State Electrochem 17(8):2283–2291

57. Pandey GP, Liu T, Hancock C, Li Y, Sun XS, Li J (2016) Thermostable gel polymer electrolyte based on succinonitrile and ionic liquid for high-performance solid-state supercapacitors. J Power Sources 328:510–519

58. Alarco PJ, Lebdeh YA, Abouimrane A, Armand M (2004) The plastic-crystalline phase of succinonitrile as a universal matrix for solid-state ionic conductors. Nat Mater 3(7):476–481

59. MacFarlane DR, Forsyth M (2001) Plastic crystal electrolyte materials: new perspectives on solid state ionics. Adv Mater 13(12-13): 957–966

60. Pringle JM (2013) Recent progress in the development and use of organic ionic plastic crystal electrolytes. Phys Chem Chem Phys 15(5):1339–1351

61. Howlett PC, Ponzio F, Fang J, Lin T, Jin L, Iranipour N, Efthimiadis J (2013) Thin and flexible solid-state organic ionic plastic crystal–polymer nanofiber composite electrolytes for device applications. Phys Chem Chem Phys 15(33):13784–13789

62. Wang X, Zhu H, Greene GW, Zhou Y, Masahiro Y-F, Miyachi Y, Armand M, Forsyth M, Pringle JM, Howlett PC (2017) Organic ionic plastic crystal-based composite electrolyte with surface enhanced ion transport and its use in all-solid-state lithium batteries. Adv Mater Tech 2:1700046

63. Chimdi T, Gunzelmann D, Vongsvivut J, Forsyth M (2015) A study of phase behavior and conductivity of mixtures of the organic ionic plastic crystal N-methyl-N-methyl-pyrrolidinium dicyanamide with sodium dicyanamide. Solid State Ionics 272:74–83

64. Chodankar NR, Dubal DP, Gund GS, Lokhande CD (2016) A symmetric MnO₂/MnO₂ flexible solid-state supercapacitor operating at 1.6 V with aqueous gel electrolyte. J Energy Chem 25(3):463–471

65. Lee K-T, Lee J-F, Wu N-L (2009) Electrochemical characterizations on MnO₂ supercapacitors with potassium polyacrylate and potassium polyacrylate-co-polyacrylamide gel polymer electrolytes. Electrochim Acta 54(26):6148–6153

66. Long S, MacFarlane DR, Forsyth M (2004) Ionic conduction in doped Succinonitrile. Solid State Ionics 175(1-4):733–738

67. Eijck LV, Best AS, Long S, Fernandez-Alonso F, MacFarlane DR, Forsyth M, Kearley GJ (2009) Localized relaxational dynamics of Succinonitrile. J Phys Chem C 113(33):15007–15013

68. Ghodbane O, Pascal J-L, Favier F (2009) Microstructural effects on charge-storage properties in MnO₂-based electrochemical supercapacitors. ACS Appl Mater Interfaces 1(5):1130–1139

69. Xiao W, Xia H, Fuh JYH, Lu L (2009) Growth of single-crystal a-MnO₂ nanotubes prepared by a hydrothermal route and their electrochemical properties. J Power Sources 193(2):935–938

70. Wei W, Cui X, Chen W, Ivey DG (2011) Manganese oxide-based materials as electrochemical supercapacitor electrodes. Chem Soc Rev 40(3):1697–1721

71. Wang J-G, Kang F, Wei B (2015) Engineering of MnO₂-based nanocomposites for high-performance supercapacitors. Prog Mater Sci 74:51–124

72. Marsh H, Rodriguez-Reinonso F (2006) Activated carbon. Elsevier Science & Technology Books, Amsterdam

73. Pal P, Pahari SK, Giri AK, Bajaj HC, Panda AB (2013) Hierarchically order porous lotus shaped nano-structured MnO₂ through MnCO₃: chelate mediated growth and shape dependent improved catalytic activity. J Mater Chem A 1:10251–10258

74. Das M, Bhattacharyya KG (2014) Oxidation of rhodamine B in aqueous medium in ambient conditions with raw and acid-activated MnO₂, NiO, ZnO as catalysts. J Mol Catal A Chem 391:121–129

75. Retter U, Widmann A, Siegler K, Kahlert H (2003) On the impedance of potassium nickel(II) hexacyanoferrate(II) composite electrodes-the generalization of the Randle's model referring to inhomogeneous electrode. J Electroanal Chem 546:87–96

76. Kumar Y, Pandey GP, Hashmi SA (2012) Gel polymer electrolyte based electrical double layer capacitors: comparative study with multiwalled carbon nanotubes and activated carbon electrodes. J Phys Chem C 116(50):26118–26127

77. Miller JR (1998) 8th international seminar on double layer capacitor and similar energy storage devices. Deerfield Beach Florida

78. Taberna P-L, Simon P, Fauvarque JF (2003) Electrochemical characteristics and impedance spectroscopy studies of carbon-carbon supercapacitors. J Electrochem Soc 150(3):A292–A300

79. Nam H-S, Kwon JS, Kim KM, Ko JM, Kim J-D (2010) Supercapacitive properties of a nanowire-structured MnO₂ electrode in the gel electrolyte containing silica. Electrochim Acta 55(25):7443–7446

80. Bharate BG, Hande PE, Samui AB, Kulkarni PS (2018) Ionic liquid (IL) capped MnO₂ nanoparticles as an electrode material and IL as electrolyte for supercapacitor application. Renew Energy 126:437–444

81. Chodankar NR, Dubal DP, Lokhande AC, Lokhande CD (2015) Ionically conducting PVA–LiClO₄ gel electrolyte for high performance flexible solid state supercapacitors. J Colloid Interface Sci 460:370–376

82. Obeidat A, Gharaibeh MA (2018) Electrochemical performance of MnO$_2$ for energy storage supercapacitors in solid-state design. Inter J Renew Energy Res 8:1229–1235

83. Wu L, Li R, Guo J, Zhou C, Zhang W, Wang C, Huang Y, Li Y, Liu J (2013) Flexible solid-state symmetric supercapacitors based on MnO$_2$ nanofilms with high rate capability and long cyclability. AIP Adv 3(8):082129

84. Zhao X, Hou Y, Wang Y, Yang L, Zhu L, Cao R, Sha Z (2017) Prepared MnO$_2$ with different crystal forms as electrode materials for supercapacitors: experimental research from hydrothermal crystallization process to electrochemical performances. RSC Adv 7(64):40286–40294